Hindawi
Structural Control and Health Monitoring
Volume 2024, Article ID 2716156, 16 pages
https://doi.org/10.1155/2024/2716156

Research Article

Enhanced Strain Measurement Sensitivity with Gold Nanoparticle-Doped Distributed Optical Fibre Sensing

Xiang Wang, Yuzhe Xiao, Calvin Rans, Rinze Benedictus, and Roger M. Groves

Faculty of Aerospace Engineering, Delft University of Technology, Delft, Netherlands

Correspondence should be addressed to Roger M. Groves; r.m.groves@tudelft.nl

Received 12 February 2023; Revised 3 February 2024; Accepted 15 March 2024; Published 2 April 2024

Academic Editor: Suparno Mukhopadhyay

Nanoparticle- (NP-) doped optical fibres show the potential to increase the signal-to-noise ratio and thus the sensitivity of optical fibre strain detection for structural health monitoring. In this paper, our previous experimental/simulation study is extended to a design study for strain monitoring. 100 nm spherical gold NPs were randomly seeded in the optical fibre core to increase the intensity of backscattered light. Backscattered light spectra were obtained in different wavelength ranges around the infrared C-band and for different gauge lengths. Spectral shift values were obtained by cross-correlation of the spectra before and after strain change. The results showed that the strain accuracy has a positive correlation with the relative spectral sensitivity and that the strain precision decreases with increasing noise. Based on the simulated results, a formula for the sensitivity of the NP-doped optical fibre sensor was obtained using an aerospace case study to provide realistic strain values. An improved method is proposed to increase the accuracy of strain detection based on increasing the relative spectral sensitivity, and the results showed that the error was reduced by about 50%, but at the expense of a reduced strain measurement range and more sensitivity to noise. These results contribute to the better application of NP-doped optical fibres for strain monitoring.

1. Introduction

Fibre optic sensors (FOS) offer an attractive option for strain sensing, which can be used for structural health monitoring (SHM) decision-making. Structural damage will cause departures in the strain field after loading [1]. The presence or position of damage can be obtained by analysing the strain information continuously. Compared with electrical strain gauges, FOS have the advantages of resistance to corrosion [2], immunity to electromagnetic interference [3], and their small size and low weight make them suitable to embed in composite materials [2]. They can also measure temperature [4], chemical parameters (pH, relative humidity) [5], material degradation [6], vibration [7], and load [8]. Because of these advantages, FOS has been used for SHM in fields such as aerospace engineering (for example, SHM in aerospace structures [9, 10]) and civil engineering (for example, the monitoring of the railway infrastructures [11] and the pavement layers [12]). The most commonly used optical fibre sensing methods for SHM include distributed fibre optic sensing [13] and fibre Bragg gratings sensing [14, 15]. Compared with fibre Bragg gratings, distributed fibre optic sensors (DFOS) have the advantage that they can obtain strain information along the length of the sensing fibres. One type of DFOS is based on the working principle of Rayleigh backscattering, where spectral wavelength shifts of the backscattered light in the optical fibre under strain are used to obtain the strain change values [13]. Combined with the optical frequency domain reflectometry (OFDR) method [16], this allows the distributed strain information to be demodulated. High spatial resolution distributed strain sensing based on Rayleigh scattering was developed by [13] with a strain resolution of 5 $\mu\epsilon$ and a spatial resolution of 30 cm. It has since been developed to have a strain resolution of up to 1 $\mu\epsilon$ with a spatial resolution of up to 1 cm [17] and has been developed for long-distance (more than 300 m) detection [18]. There are plenty of applications of DFOS for SHM, for example, damage detection for a carbon fibre reinforced plastic (CFRP) beam and a composite wing [19] and the state sensing of a composite winglet structure [20].

The strain measurement performance of a DFOS directly determines the final performance of SHM, and high-performance sensing is beneficial to SHM [21]. Some drawbacks restrict the application of DFOS for some applications. The durability of the optical fibre sensor in engineering has drawn researchers' attention [22]. The strain transfer between the materials and the sensing fibre should be considered for accurate strain measurement in engineering [23]. Another limitation which restricts DFOS strain measurement based on Rayleigh backscattering has drawn many researchers' attention in recent years is that this method uses the backscattered light in the core of the optical fibres, while the Rayleigh scattering in the core of commercial optical fibres is low [24]. For a commercial optical fibre, the backscattered light signal is as low as −100 dB/mm [25]. By increasing the backscattered light in the core of the optical fibres, the signal-to-noise ratio (SNR) may increase, allowing the precision of the strain detection to increase.

Some previous research shows improvements in the strain/temperature measurement based on increasing the backscattered light signals. Loranger et al. increased the magnitude of backscattered light by 20 dB by ultraviolet laser exposure (213 nm wavelength) of the core of the optical fibres [24], and the strain/temperature measurement noise level decreased. Parent et al. achieved about 37 dB backscattered light enhancement with the ultraviolet laser exposure of the core of optical fibres and the accuracy of the shape sensing of the surgical needles increased by 47% [26]. Doping nanoparticles (NPs) into the core of the optical fibre is a direct approach to increasing the backscattered light. The engineering features of NP-doped optical fibres have been investigated for manufacturing, signal attenuation, and light enhancement with different types of NPs (MgO-based NPs [27] and Ca-based NPs [28, 29]). Gold NPs are competitive contrast agents that can increase backscattered light [30]. If gold NP-doped optical fibre is used in strain detection for SHM, a higher SNR signal may improve the precision of the strain measurement for SHM which is beneficial for critical locations. For example, critical locations include the areas close to the rivet holes in the aluminium fuselage where small cracks may form [31]. These small cracks will induce a small localised strain change compared to a healthy structure, so a high strain sensitivity is needed for detection.

In our previous work, gold NP-doped optical fibres were investigated by experiments and simulations. To investigate the backscattered light enhancement in an optical laboratory, a method of doping liquid containing gold NPs onto the optical fibre end tips was proposed to analyse the intensity of backscattered light signal scattered by the NPs [32] and analyse the spectral shift of the NP-doped optical fibres under strain experimentally [33]. By simulation, the optimised light enhancement at 1550 nm wavelength was obtained (about 64 dB) [30]. With NP-doping, the intensity of the backscattered light in the optical fibre will increase to overcome the drawback of low backscattering intensity of commercial optical fibres. A comparison between different methods of backscattered light enhancement in the core of the optical fibres is listed in Table 1, and gold NP-doped distributed fibre sensing shows the advantages of light enhancement. The NP-doped optical fibres' backscattered light spectra differ from the commercial signal mode optical fibres or fibre Bragg gratings. The new spectral characteristics of NP-doped optical fibre under strain were obtained in previous work [34].

The previous research showed that the dramatically increased backscattered light signal benefits the strain/temperature measurement [28–30]. The sensitivity is the minimum signal that can be detected and the research on sensitivity improvement is an important topic. Loranger et al. [24] performed research on the sensitivity improvement of the distributed fibre optic sensing for different gauge lengths with backscattered light enhancement method for some cases by measuring the root mean square noise. However, studying the performance of strain measurement under different noise levels for different cases experimentally is a challenge and the experimental results only showed that the signal-to-noise ratio increases from the engineering aspect. The theoretical performance of the NP-doped FOS for strain monitoring still needs to be investigated. In addition, the backscattered light spectra of NP-doped optical fibre are different from commercial optical fibres. In this case, the traditional cross-correlation method to demodulate the spectral shift under strain should be developed for a more accurate strain/temperature measurement.

In this paper, strain acquisition of gold NP-doped distributed fibre optic sensing will first be investigated with the cross-correlation method. The errors caused using the cross-correlation method for NP-doped optical fibre will be evaluated for different random-seeded optical fibre gauge lengths without noise and for the specific random-seeded optical fibre gauge lengths under different noise levels. Gaussian noise is assumed and applied to the photoelectric conversion signals. By linear fitting, the sensitivity of the NP-doped optical fibre strain gauges can be obtained. To improve the accuracy of strain detection with the cross-correlation method for NP-doped optical fibre sensors, a new method is proposed to increase the accuracy of strain detection.

The paper is organized as follows. The first section is the Introduction. The experimental setup, the principle of the measurements, and the proposed method for increasing the accuracy of spectral shift detection are illustrated in the Methodology section. The third section shows the simulation results for different random-seeded optical fibre gauge lengths without noise and for the specific random-seeded optical fibre gauge lengths under different noise levels. Analysis from the simulation and a strain measurement application (an aerospace case study) will be shown and discussed in the Analysis and Discussion section to present the sensitivity of the NP-doped optical fibre sensors and to make a comparison with the traditionally used FOS. Then, the results of the strain acquisition with the new proposed method will be discussed. The fifth section is the Conclusions section.

Table 1: Light enhancement comparison with different methods.

Method	Light enhancement (dB)	References
Ultraviolet laser exposure	20	Loranger et al. [24]
Ultraviolet laser exposure	37	Parent et al. [26]
Ultrafast laser exposure	>40	Yan et al. [35]
Gold NP-doped optical fibre sensing	64	Wang et al. [30]
Calcium-based NP-doped optical fibre sensing	25.9–44.9	Fuertes et al. [29]
Magnesium oxide NP-doped optical fibre sensing	>50	Molardi et al. [36]
Magnesium oxide NP-doped optical fibre sensing	48.9	Tosi et al. [27]

2. Methodology

2.1. Experimental Setup and the Principle. Figure 1(a) shows a simplified diagram of the optical fibre sensing system based on backscattering by the NPs. Figure 1(b) shows the structure of the strain measurement system monitoring strain distribution in a specimen under load with an optical fibre. In Figure 1(a), the optical fibre sensing system consists of a wavelength-tunable laser, optical fibre couplers, an optical fibre circulator, optical fibres, a sensing fibre containing gold NPs, a photodetector, and an optical trap. The light signals detected by the photodetector are processed by the computer which is not shown in figure.

Light emitted from the tunable laser is split by an optical coupler into sensing and reference paths. The gold NPs are randomly distributed in the sensing fibre core volume. Light is backscattered by the NPs and recoupled into the optical fibre in the backward direction. An optical trap at the end of the sensing fibre is used to reduce the reflection at the optical fibre end tip, which can be a refractive index (RI) matching liquid or a no-core optical fibre. The backscattered light passes through the optical circulator and then interferes with light from the reference arm at the optical fibre coupler. Optical beat signals obtained at the photodetector are demodulated by Fourier transform to recover the intensity and phase of the backscattered light in each gauge length.

The beat signals can be expressed as follows [38, 39]:

$$\mathrm{PD}_2 \approx \sum_i r_i(k) \cos 2n_{\mathrm{eff}} z_i k, \tag{1}$$

where r_i is the reflection coefficient at position z_i of the sensing fibre and the squared magnitude $|r_i|^2$ is the reflectance. The spatial distances between the i^{th} and the $(i+1)^{\mathrm{th}}$ detection points (spatial resolution) are determined by the effective RI of the optical fibre and the tuning wavelength range is $\Delta z = \lambda_s \lambda_f / 2n\Delta\lambda$, where λ_s is the starting wavelength of the tunable laser and λ_f is the final wavelength, $\Delta\lambda$ is the wavelength tuning range, n_{eff} is the effective RI of the optical fibre [40] and k is the wavenumber. For a tunable laser source with a starting wavelength at 1540 nm and a final wavelength at 1560 nm, the spatial resolution is about 41 nm when the RI is 1.45. If the gauge length is set at 1 mm, there are about 24 detection points in the gauge length. It can be seen from equation (1) that PD_2 contains information about the position (z_i) and the wavenumber (k) and it can be transformed by Fourier transform. Because the laser is linear tuning, the beat signals are proportional to the positions of z_i [41]. The intensity and phase of the scattered light spectra within the gauge length can be obtained by square windowing the positions within the gauge length and using an inverse Fourier transform. Then, the spectral shift can be obtained using cross-correlation between the reference spectrum and the spectrum after the strain is applied [42].

2.2. The Method of the Spectral Shift Detection by Cross-Correlation Method with Gold NP-Doped Optical Fibre. The accuracy of the cross-correlation was evaluated by comparing the theoretical spectral shift under strain and the spectral shift result from the cross-correlation method. The central wavelength of the tunable laser was set at 1550 nm. The wavelength tuning ranges were set at 10 nm, 20 nm, and 40 nm, which correspond to the wavelength ranges 1545 nm–1555 nm, 1540 nm–1560 nm, and 1530 nm–1570 nm, respectively. The simulated spectra were in the wavelength domain with a high spectral resolution of 1 pm in order to accurately reconstruct the spectra. In this case, the spectral shift (R_{xy}) was calculated by the cross-correlation method in the wavelength domain as follows:

$$R_{xy}(n) = \frac{1}{N} \sum_{m=0}^{N-1} [x(m) - \overline{x}][y(n+m) - \overline{y}], \tag{2}$$

where $n = -(N-1), -(N-2), \ldots, N-2, N-1$. N is the number of sampling points in wavelength range. The sampling points were mapped to a uniform scale in the wavelength domain. The resolution was set at 1 pm. y and x correspond to the reference spectrum and the spectrum under strain, respectively. y and x were normalised to the range of 0 to 1.

The strain was applied to the sensing fibre by a controlled load to apply force on the optical fibres. In the experiment in this paper, a controlled tensile was applied to the specimen containing an optical sensing fibre to change the strain of the sensing fibre. In this case, the relative positions of the gold NPs in the sensing fibre will change and the RI of the optical fibre will change also. The backscattered spectra from the NPs in the gauge length were modelled by a single scattering model which means the light will be backscattered once in the propagation direction and can be expressed as follows [34]:

$$\lambda'_{\mathrm{NP}} \approx \lambda_{\mathrm{NP}} \left(1 + \varepsilon_{\mathrm{fibre}} + \eta_m \varepsilon_{\mathrm{fibre}}\right), \tag{3}$$

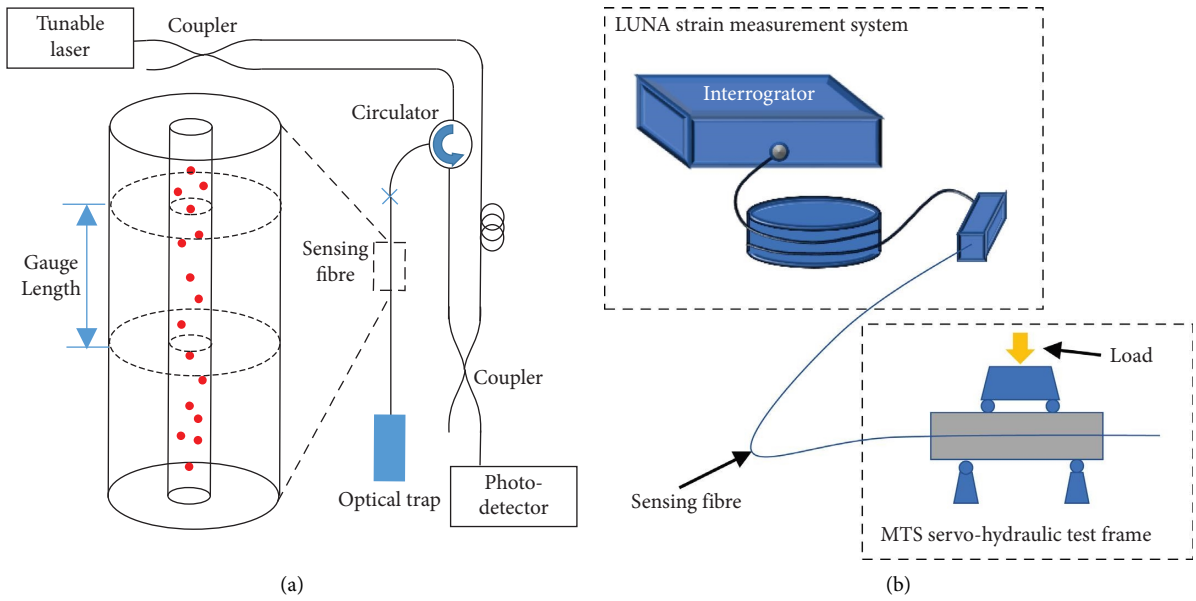

FIGURE 1: The structure of the experimental setup. (a) The structure of the distributed fibre optic sensing system. The red dots show gold NPs randomly distributed in the core of the optical fibre. The outer layers are the cladding and coating. (b) The structure of the strain measurement system [37] with a specimen under load.

where λ'_{NP} is the spectrum under strain and λ_{NP} is the reference spectrum. $\eta_m = -(p_{12} - \nu(p_{11} + p_{12}))n^2/2$ which is the parameter caused by the RI change under strain [43]. When $\nu = 0.17$ [44], $p_{11} = 0.113$, $p_{12} = 0.252$ [44], and $n = 1.45$ for the optical fibre, $\eta_m = -0.1997$. Therefore, the theoretical spectral shift under strain is $1.240465\,\text{pm}/\mu\epsilon$ which was set as the true value used to compare with the simulated results.

From the previous work, low-concentration NP-doping shows similar spectral characteristics in the wavelength and wave number domains [34] for different sizes of NPs. To simplify the simulation, only 100 NPs (100 nm diameter) were randomly seeded in the gauge lengths for a low concentration of NP doping. The amplitudes of the scattered light were calculated with Mie theory. Once the NPs have been seeded, the spectral intensity can be expressed by the square of the accumulation of the electric field caused by the scattering from the NPs as follows [34]:

$$I_s(\lambda) \approx \left| \sum_{i=1}^{N} E_0 A_i \exp\left(j \frac{4\pi n_m l_i}{\lambda} (1 + \varepsilon + \eta_m \varepsilon) \right) \right|^2, \quad (4)$$

where E_0 is the electrical field of the incident light, $A_i = r(l_i)\exp(-6\pi f n_m \Re S(0) l_i/\lambda x^3)$, $r(l_i)$ is the reflection coefficient of the NP at position of l_i in the backward direction in the optical fibre which is calculated with Mie theory, f is the volume ratio of gold NP in the optical fibre, n_m is the RI of the optical fibre, $\Re$ is the real symbol, $S(0)$ is the forward scattering amplitude, λ is the wavelength of the incident light, x is the size parameter of the gold NP, j is the imaginary unit, and ε represents axial strain.

The simulations of the backscattered light spectra were performed analytically and the simulation procedure is shown in Figure 2. Figure 2(a) shows the structure of the tested optical fibre. The incident light propagates through the optical fibre gauge length and is scattered by the randomly seeded NPs in the core. The output signal is the accumulation of scattered light signals within the gauge length. The procedure for calculating the strain values is shown in Figure 2(b). First, the NPs were seeded at random positions in the gauge. The backscattered light spectra were calculated based on equation (4), where the Mie theory and numerical aperture were applied to the simulations. The spectral shift values and then the strain values were calculated with the cross-correlation method. To analyse the relative spectral sensitivity, the backscattered light spectra can be transferred to spatial frequency $(1/\lambda)$ by Fourier transform to evaluate the fluctuation within 1 nm. In order to obtain this fluctuation, a threshold was set at $1/e$ of the maximum value in the spatial frequency domain. The first spatial frequency value over the threshold from half of its maximum spatial frequency to the low spatial frequency was chosen as its fluctuation number was within 1 nm. Note: the spectra were normalised to the range 0-1 and were then subtracted from the mean values of the spectra.

The parameters used for the simulations are shown in Table 2. In the simulation, the geometry of the optical fibres was cylinders. The gauge lengths were chosen to be integer multiples of the grating period of the fibre Bragg gratings for a wavelength at 1550 nm for a separate study. The reasons for choosing the strain range ($-3000\,\mu\epsilon$ to $3000\,\mu\epsilon$) and strain interval ($100\,\mu\epsilon$) are that it is a relatively wide strain range to cover the strain values in the loading test for the specimen in this paper and the strain interval's choosing has balanced the time-consuming and resources consuming for the computing. The number of the NPs in the core of the optical fibre was set at 100. The reason for choosing 100 NPs is that 1: it is a very low concentration and it meets the single scattering

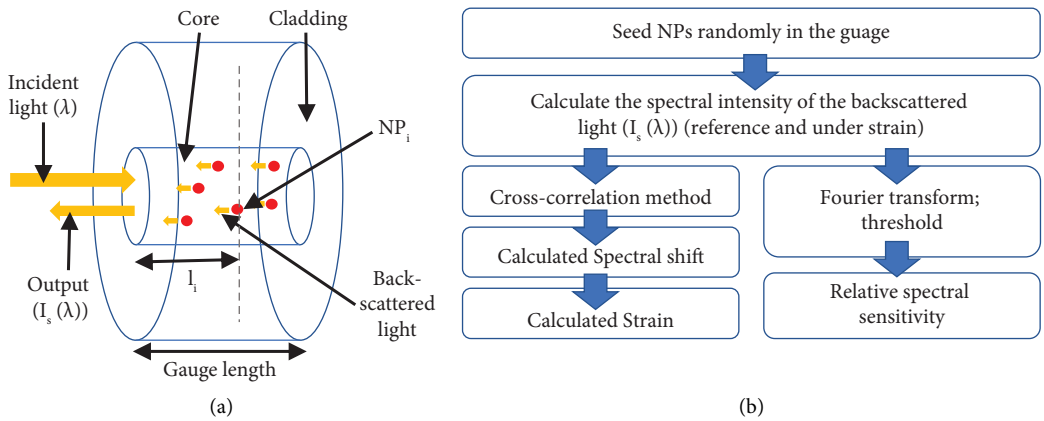

Figure 2: The procedure of the simulations. (a) The structure of the tested optical fibre. (b) Calculation procedure's blocks.

Table 2: The parameters used for the simulations.

Parameter	Value
Diameter of the core of the optical fibre	9.5 μm
Numerical aperture of the optical fibre	0.13 at 1550 nm (1550BHP, Thorlabs)
Gauge lengths	0.1069 cm, 0.2138 cm, 0.3207 cm, 0.4276 cm, 0.5345 cm, 0.6414 cm, 0.7483 cm, 0.8552 cm, 0.9621 cm, and 1.0690 cm
Strain range	$-3000\,\mu\epsilon$ to $3000\,\mu\epsilon$
Strain interval	$100\,\mu\epsilon$
Number of the NPs	100
Wavelength ranges (λ)	1545–1555 nm, 1540–1560 nm, and 1530–1570 nm

assumption ($l < 1/c/C_{ext}$, where l here is the gauge length, c is the concentration of the NPs and C_{ext} is the extinction cross-section for the NP which can be calculated by Mie theory) for the set gauge lengths; 2: the spectral characteristics show similarities when it meets the single scattering requirement according the results from the research [34]. In this case, the generated spectra are general and can also be valid for other concentration cases. The results also apply to other sizes of NPs, even though the sizes of the NPs were set at 100 nm in this paper.

2.3. A New Method for Increasing the Accuracy of Spectral Shift Detection. It was found that the accuracy of the cross-correlation relies on the characteristic spectral peaks. For the cases of shorter gauge lengths (see Simulation Results section), the spatial frequency is less than the cases of longer gauge lengths. It means that the characteristic spectral peaks of the shorter gauge lengths are less than the cases of the longer gauge lengths, which will lead to the lower accuracy of spectral shift monitoring for short gauge lengths with the cross-correlation method. Based on this, in this section, a method to increase the accuracy of spectral shift monitoring based on increasing the spatial frequency is proposed.

The method to increase the characteristic spectral peaks is using partial spectral inversion. The spectra processing procedures are as follows: Firstly, the original spectra were normalised to the range 0-1 (x and y). Secondly, the direct current part of the normalised spectra was deduced by subtracting their mean values ($x(m) - \overline{x}$ and $y(n+m) - \overline{y}$). Then, the values of the spectra are around zero. Thirdly, by spectra inversion operation of the spectra below zero ($|x(m) - \overline{x}|$) and $|y(n+m) - \overline{y}|$)), the absolute values of the spectra were obtained. Fourthly, the direct current part of the normalised spectra was deduced by subtracting their mean values ($\overline{|x(m) - \overline{x}|}$ and $\overline{|y(n+m) - \overline{y}|}$). The final step is using the cross-correlation method for the processed reference spectrum and the spectrum under strain to obtain the spectral shift. By a spectra inversion operation, additional high-frequency information was added to the original spectra.

The proposed method can be expressed as follows:

$$R'_{xy}(n) = \frac{1}{N}\sum_{m=0}^{N-1}\left(|x(m) - \overline{x}| - \overline{|x(m) - \overline{x}|}\right) \cdot \left(|y(n+m) - \overline{y}| - \overline{y(n+m) - \overline{y}|}\right), \quad (5)$$

where N is the number of the wavelengths used for calculation, x and y refer to the normalised reference spectrum and the spectrum under strain respectively. $\overline{x}$ and $\overline{y}$ are the mean values of the reference spectrum and the spectrum under strain, respectively.

A case for the spectra generated by 100 nm size gold NPs randomly distributed in the optical fibre is shown in Figure 3. The gauge length was set at 0.3207 cm. The spectral range was set from 1545 nm to 1555 nm. The wavelength resolution was set at 1 pm.

In Figure 3(a), the reference spectrum is shown by blue lines and the spectrum under strain at $-1200\,\mu\epsilon$ is shown by black lines. The spectrum under strain shows a left spectral shift when it is compared with the reference spectrum. The black arrow shows the direction of the spectral shift of one of its major characteristic spectral peaks. The characteristics of the spectral shift under strain of the NP-doped optical fibre show similar spectral shift characteristics of fibre Bragg gratings but the characteristic peaks are quite different from the Bragg peaks. In order to show the characteristics of the fluctuation of the peaks, the Fourier transform is applied to the backscattered light spectra to show the number of fluctuations of the spectra within one wavelength (relative spectral sensitivity). The results of the spectra shown in Figure 3(a) after the Fourier transform are shown in Figure 3(b). Half of the sampling frequency is 500/nm, which is much larger than the 3 dB frequency of the spatial frequency. In this case, the sampling rate is two times larger than the Nyquist frequency. Therefore, the spectral information can be recovered with this resolution. The results after Fourier transforms in Figure 3(b) have been reduced by subtracting the direct current component in Figure 3(a). The traditional cross-correlation method is used for the spectral shift measurement with the spectra in Figure 3(a).

Figure 3(c) shows the processed spectra with the proposed method. Figure 3(d) shows the intensity information after the Fourier transform. Compared with Figure 3(a), with the new method, the characteristic peaks in Figure 3(a) increase. In this case, the relative spectral sensitivity increases which can be seen in Figure 3(d). There are more high-frequency components shown in Figure 3(d) than the results in Figure 3(b) for both the reference spectrum and the spectrum under strain. The corresponding spatial frequency at the threshold $(1/e)$ may be different for the reference spectrum and the spectrum under strain because some of the major characteristic peaks may move outside the measured spectral range. In addition, the obtained spatial frequencies after the Fourier transform are discrete values. Therefore, the end point (the nearest spatial frequency at which the intensity of the result after the Fourier transform is above the threshold) is used for the reference spectrum to compare the fluctuation of the spectra used in traditional cross-correlation method and the new method. With the new method, the spatial frequency at the end point increases when comparing Figure 3(d) ($2.4\,\text{nm}^{-1}$) and Figure 3(b) ($1.6\,\text{nm}^{-1}$), which will be beneficial for a more accurate strain measurement (in Results of the newly proposed method in the Analysis and Discussion section).

In this work, the performance of the strain monitoring of signal-enhanced distributed fibre optical sensing based on backscattering by doping gold NPs will be investigated by simulations with a single scattering model in order to improve the sensing performance. The simulation results of the NP-doped optical fibre sensors will be shown in the next section.

3. Simulation Results

The results of the cases of the accuracy of the spectral shift acquisition based on the cross-correlation method will be shown. The first three cases were generated by 100 times random seeding NPs without noise for different gauge lengths. The following three cases were generated with the same selected random seeding NPs distribution with different noise levels and different gauge lengths to assess the accuracy with the cross-correlation method used for NP-doped optical fibre sensors.

3.1. Spectral Analysis with 100 Random Seedings without Noise. Figure 4 shows the strain errors between the simulated and theoretical results. The simulated results were obtained with the cross-correlation method to calculate spectral shifts under strain for spectral detection ranges 10 nm, 20 nm, and 40 nm with the central wavelength of 1550 nm in Figures 4(a)–4(c), respectively. The true values (theoretical results) were obtained by using the theoretical response of the spectral shift ($1.240465\,\text{pm}/\mu\epsilon$) multiplied by the strain values. The strain range was set from $-3000\,\mu\epsilon$ to $3000\,\mu\epsilon$ and the strain interval was set at $100\,\mu\epsilon$. The gauge lengths were set at 0.1069 cm, 0.2138 cm, 0.3207 cm, 0.4276 cm, 0.5345 cm, 0.6414 cm, 0.7483 cm, 0.8552 cm, 0.9621 cm, and 1.0690 cm, respectively.

To show the ratios of the deviation between the calculated mean values and the true values, the relative error is defined as follows:

$$E_r = \left|\frac{\text{calculated result} - \text{true value}}{\text{true value}} \times 100\%\right|. \quad (6)$$

The relative errors between mean values and the true values are shown in Figures 4(a-1)–4(c-1). They were obtained by averaging the 100 cases of the obtained errors. Because equation (6) cannot be used for the cases for strain at 0, the results close to strain at 0 are not available.

In the small gauge length ranges, as seen from Figure 4(a-1), the calculated mean spectral shifts were not sufficient to reach the true spectral shifts, especially for larger strain values. A reason for this may be that a large strain causes a large spectral shift and a larger spectral shift causes a higher percentage of the spectrum moving out of the spectral detection range and being replaced by a new spectrum and the new spectrum has no correlation with any regions of the original spectrum. The high errors shown in Figure 4(a-1) represent the failure of strain acquisition with the cross-correlation method. To show the degree of dispersion of the 100 randomly seeding cases, the errors calculated with the minimum data and the

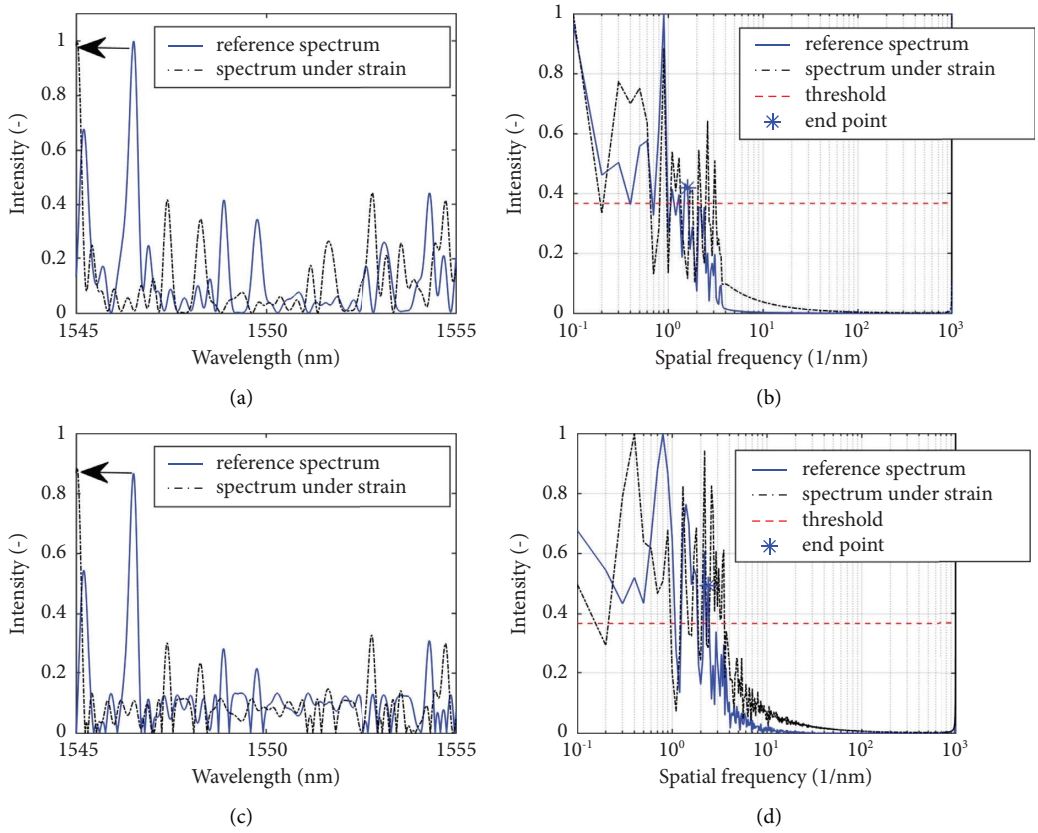

FIGURE 3: A case of the spectra of the random distribution of NPs in the optical fibre with a gauge length of 0.3207 cm for strain at $-1200\,\mu\epsilon$. (a) The original spectrum and spectrum under strain. (b) The results of the spectra with Fourier transform. The black arrows show the spectral shift directions under $-1200\,\mu\epsilon$. (c) The spectra modulated by the proposed method. (d) The results of the modulated spectra with Fourier transform. The black arrows show the spectral shift directions under $-1200\,\mu\epsilon$ [45].

maximum data in the 100 cases for each gauge length and strain were compared with the true values shown in Figures 4(a-2) and 4(a-3), respectively. A threshold of 20% was set for both figures to show the regions where the errors are above 20% and more details about the regions where the errors are below 20%. It is interesting to see that significant errors only exist in positive strain regions in Figure 4(a-2) for the calculated minimum errors and only exist in negative strain regions in Figure 4(a-3) for the calculated maximum errors. This indicates that some cases failed when the cross-correlation method was used. Figure 4(a-4) shows the standard deviations of strain errors. The white line shows a boundary around the threshold in Figure 4(a-4) and the white line passes through ($0\,\mu\epsilon$, 0 cm) and ($2300\,\mu\epsilon$, 1.0690 cm). The boundary lines shown in Figure 4(b-4) pass through ($0\,\mu\epsilon$, 0 cm) and ($-2000\,\mu\epsilon$, 1.0690 cm). The two white lines were also drawn in Figure 4(a-4) and similar boundaries are shown when the threshold was set at 0.5%. The standard deviations are quite small but the errors calculated with the maximum results and minimum results shown in Figures 4(a-2) and 4(a-3) are large, which also indicates a failure of the spectral shift acquisitions with the cross-correlation method and indicates that the failure cases have a low proportion for the 100 randomly cases.

Figures 4(b-1)–4(b-3) show errors between the mean values and the theoretical values, the errors between the minimum calculated results and the theoretical values, and the errors between the maximum calculated results and the theoretical values, respectively. The errors between the mean values and the theoretical values shown in Figure 4(b-1) are small compared with the results in Figure 4(b-1). Only the regions close to the smallest gauge lengths for some large strain values show high error values. Because the relative errors are quite small, the threshold was set at 2% for the results shown in Figures 4(b-2) and 4(b-3). With the 2% error threshold, the regions of the errors above the threshold are similar to the regions of the errors above the threshold of 20% shown in Figures 4(a-2) and 4(a-3). Figure 4(b-4) shows the standard deviations of strain errors. In Figure 4(b-4), the errors are reduced to lower values compared with Figure 4(a-4), especially for the regions for larger strain and small gauge length. However, errors still exist in regions with a small strain and a small gauge length. Figure is not symmetric as can be seen from the dark blue and light blue zones in Figure 4(b-4). The reason for this is unclear and needs to be investigated further.

The results for the 40 nm spectral detection range (1530 nm–1570 nm) case are shown in Figure 4(c). Figures 4(c-1)–4(c-4) show the errors between the mean

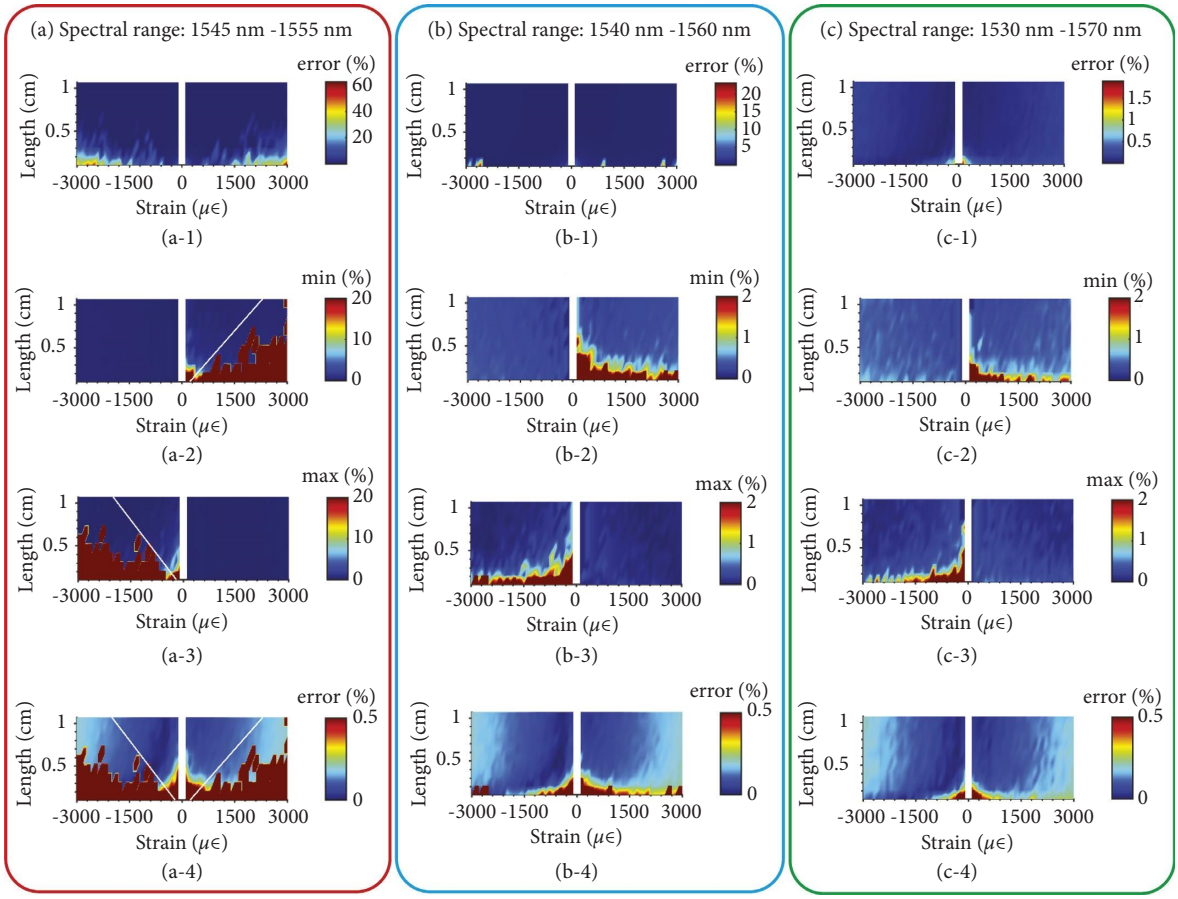

Figure 4: The errors of the strains. The cross-correlation results for the spectral range of (a) 10 nm, (b) 20 nm, and (c) 40 nm. The numbers (−1, −2, −3, and −4) in figures (a–c) correspond to the relative errors between the mean values and true values, the relative errors between the minimum values and the true values, the relative errors between the maximum values and the true values, and the relative errors between the mean values and true values with a threshold error of 0.5%, respectively [45].

values and the theoretical values, the errors between the minimum calculated results and the theoretical values, the errors between the maximum calculated results and the theoretical values and the standard deviations of strain errors, respectively.

The errors between the mean values and the theoretical values in Figure 4(c-1) are smaller than the results shown in Figures 4(a-1) and 4(b-1). Only the regions close to the smallest gauge lengths show high error values. The threshold was set at 2% for the results shown in Figures 4(c-2) and 4(c-3) which is the same as the threshold in Figures 4(b-2) and 4(b-3). The threshold set in Figure 3(c-4) was 0.5%. With the same thresholds, it can be seen that the errors decrease when the spectral ranges increase.

The above results show the randomly positioned NP cases and the corresponding statistical results for different spectral ranges without noise. In the following part, different levels of random intensity noise will be added to the spectral signals obtained from a random spatial distribution in the same gauge lengths, strain ranges and spectral ranges. The failure caused by the cross-correlation was avoided in this selected NP relative spatial distribution.

3.2. Spectral Analysis with a Specific Random Seeding with Noise. Figure 5(a) shows the direct errors between the mean values of the spectral shifts calculated with the cross-correlation method with different noise levels. The strain values can be obtained by using the theoretical response of the spectral shift. The direct error was defined as follows:

$$E_d = \text{calculated result} - \text{true value}. \tag{7}$$

The mean values were the averaged results of 100 spectra superposed with randomly generated noise. The noise is assumed to follow a Gaussian distribution with a mean value of 0 and a standard deviation of σ_n. The noise level in the simulation was defined as follows:

$$N = \frac{\sigma_n}{\max\{I_s\}}, \tag{8}$$

where $\max\{I_s\}$ represents the maximum value of the original backscattered light spectrum without noise in the gauge lengths. It is assumed that σ_n is independent of the intensity of the signal. Figures 5(a-1)–5(a-3) show the errors between

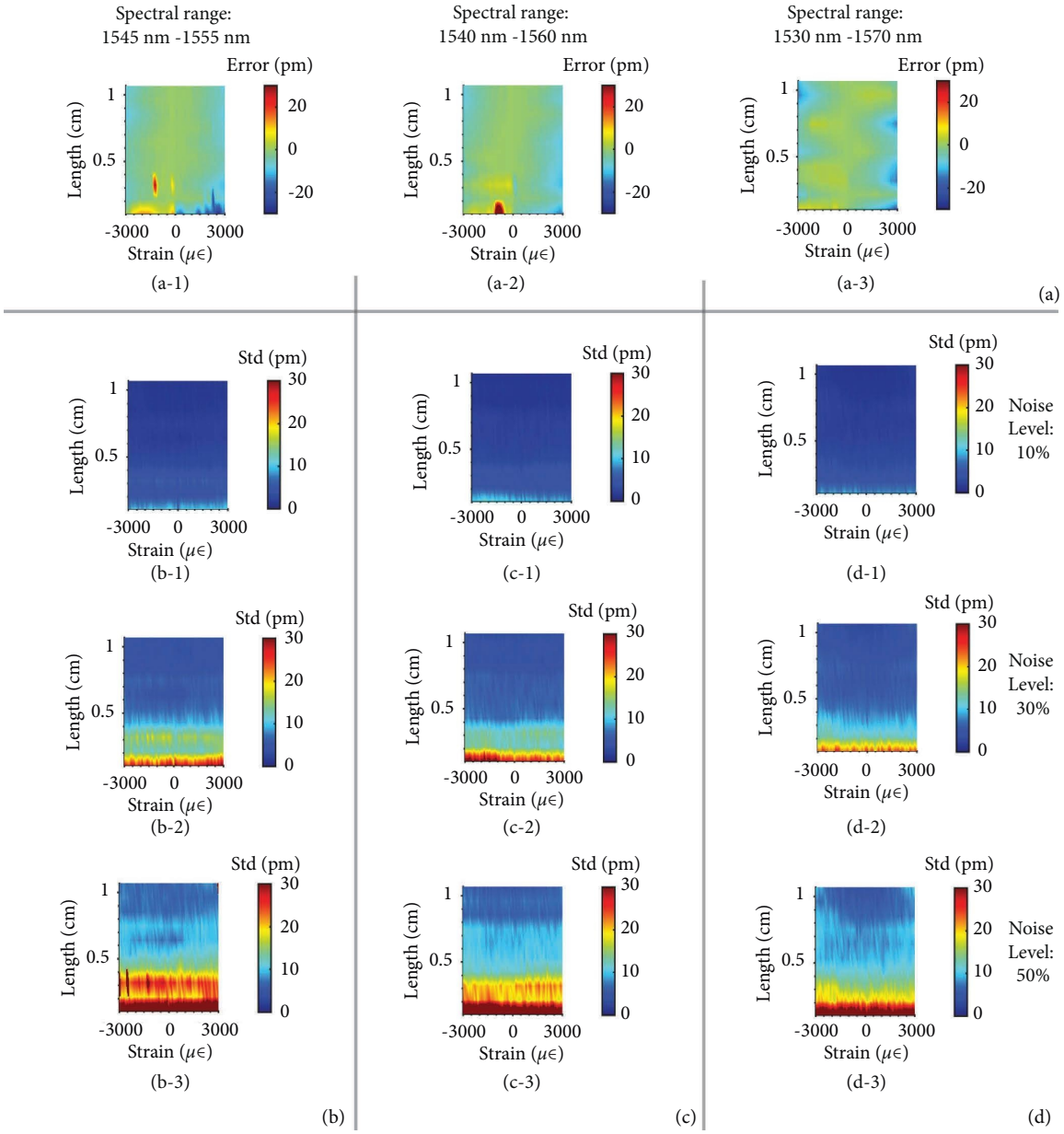

FIGURE 5: The simulated results of strain acquisition. (a-1–a-3) The errors between the spectral shift obtained and the theoretical results for spectral ranges of 10 nm, 20 nm, and 40 nm, respectively. (b and c) The standard deviations of the spectral shift for spectral ranges of 10 nm, 20 nm, and 40 nm, respectively. The numbers (–1, –2, and –3) for figures (b–d) correspond to results under noise levels of 10%, 30%, and 50%, respectively [45].

the mean values of the spectral shifts calculated with the cross-correlation method under noise levels of 0% for spectral ranges of 10 nm, 20 nm, and 40 nm, respectively. (The results for noise levels of 10%, 20%, 30%, 40%, and 50% are not shown because noise shows no influence on the mean values).

The original spectrum without noise was normalised to 0-1 and then noise with noise level N was added to the original spectrum. By setting the noise level, spectra with different noise levels can be simulated. In this case, the approximated SNR ratio can be expressed as follows:

$$\mathrm{SNR}_L = \frac{\max\{I_s\}^2}{\sigma_n^2}, \tag{9}$$

or as SNR_L ratio in dB as follows:

$$\mathrm{SNR}_{L_{\mathrm{dB}}} = 10\log\frac{\max\{I_s\}^2}{\sigma_n^2}. \tag{10}$$

Figure 5(a) shows the errors between the calculated values and the true values for 10 nm, 20 nm, and 40 nm spectral ranges, respectively. In Figure 5(a-1), the errors

between the calculated values and the true values become notable when the gauge lengths are small. There is a noticeable error around the point (−1200 $\mu\epsilon$, 0.3207 cm). The reason for this noticeable error can be illustrated with the spectra shown in Figure 3(a). Figure 3(a) shows the corresponding spectrum for the strain at −1200 $\mu\epsilon$ and for the gauge length set at 0.3207 cm. Under the strain value of −1200 $\mu\epsilon$, the original spectrum in blue has a blue shift. The arrow shows the spectral shift under this strain value and the spectrum under this strain value was in green. As shown in Figure 3(a), there is a distinguishable peak near the arrow and the intensity of the peak is much larger than the other peak values shown in the spectral range. Therefore, the shift of this peak has a high influence on calculating the spectral shift under strain with the cross-correlation method. For the strain value at −1200 $\mu\epsilon$, the peak shifts out of the spectral range which is a reason for the high error near this point shown in Figure 3(a). This result indicates that the accuracy of obtaining the spectral shift not only depends on the gauge lengths and the strain ranges but the accuracy also depends on the characteristics of the original spectrum. Figures 5(a-2) and 5(a-3) show smaller errors than errors in Figure 5(a-1), but the characteristics of the original spectrum depend on the distribution of the NPs. For example, in Figure 5(a-2) a remarkable error occurs at negative strain and the shortest gauge length for calculation. The positions of the high error points depend on the characteristics of the original spectrum. By adjusting the spectral range, the high error points can be moved.

Figures 5(b)–5(d) show the standard deviations of the spectral shift obtained with the cross-correlation method with the same random NP seeding distribution in the gauge lengths with the 10 nm, 20 nm, and 40 nm spectral range under different noise levels (10%, 30%, and 50%), respectively. As the noise level increases, the standard deviations increase especially for the short gauge lengths. For a specific noise level, the standard deviations of the results caused by the noise are similar for different strain values. The standard deviation shows a positive relevant relationship with the noise level.

4. Analysis and Discussion

In the previous subsections for different spectral ranges with random seedings, the results for the accuracy of spectral shifts demodulation with cross-correlation method were shown. The value of spectral shift times the theoretical responsivity of strain (about 1.24 pm/$\mu\epsilon$) is the obtained strain results. By increasing the detected spectral range, the accuracy of the strain acquisition increases with the cross-correlation method. Although these results show the tendency of some relationships, the mathematical relationship between parameters (for example, spectral range, and gauge length) is unclear. The failure of the strain acquisition shown in the results of subsections of spectral range 1545 nm to 1555 nm with random seedings, spectral range 1540 nm to 1560 nm with random seedings and spectral range 1530 nm to 1570 nm with random seedings causes difficulty to obtain a formula to show the relationships, so the results from the subsections of spectral ranges 1545 nm to 1555 nm, 1540 nm to 1560 nm, and 1530 nm to 1570 nm with the specific random seedings are used for further analysis since these results show the strain acquisition without failure.

In this section, further analysis of the parameters (spectral range, gauge length, and signal-to-noise ratio) will be investigated in order to obtain a formula for evaluating the sensitivity of the NP-doped optical fibre sensors. This is followed by an aerospace case study of real strain data obtained by LUNA system (ODiSI-B) with commercial optical fibres which is used as a comparison with the simulated results from NP-doped optical fibre sensors. Finally, the results of the proposed new spectral shift demodulation method are shown and discussed.

4.1. Sensitivity of the NP-Doped Optical Fibre Sensors. Figure 6 shows the relationship between the reciprocal of spatial frequency and the modified standard deviation of the cross-correlation method. The horizontal axis is the reciprocal of spatial frequency (R) and the vertical axis is the modified standard deviation (M). They show an approximate linear relationship, which will be easier for linear or polynomial fitting.

There are 15 groups of data shown in Figure 6. The datasets with the spectral ranges 10 nm, 20 nm and 40 nm are shown in red, blue and green respectively. The dataset with noise levels of 10%, 20%, 30%, 40%, and 50% are shown with a pentagram, asterisk, plus sign, circle and a triangle, respectively. The reason that there is no data shown in Figure 6 with a noise level of 0 is that the signal-to-noise ratio is finite when the noise is 0 and the modified standard deviation was defined as $M = D/N$. D represents the standard deviation of the obtained spectral shift and N is the noise level. In this case, the standard deviation is always 0 for the noise level of 0. The reason for using modified standard deviation rather than standard deviation is that standard deviation cannot be distinguished when the noise level is small. By dividing the noise level, the modified standard deviation can be shown in an approximated linear function, although the deviation may be large for small noise levels.

By a linear fitting, a relationship between the modified standard deviation and the reciprocal of spatial frequency can be found ($R^2 = 0.8993$):

$$M = 59.2457R + 14.3808. \tag{11}$$

The reciprocal of spatial frequency (R) is defined as $R = 1/F$. F is the spatial frequency of the spectrum after the Fourier transform which meets the threshold of $1/e$ which is defined as the first spatial frequency point that is over the threshold of $1/e$ and this first point was chosen from the high frequency, beginning with half of the total spatial frequency after the Fourier transform to lower frequencies. $F = P/W$, where P is the spatial frequency in the spectral range and W is the wavelength range with the unit of nm. Along with the definition of SNR as $\mathrm{SNR}_L = 1/N^2$, the relationship between the noise level, the spectral range, the gauge length, the standard deviation of the calculated spectral shift with the cross-correlation method can be expressed as follows:

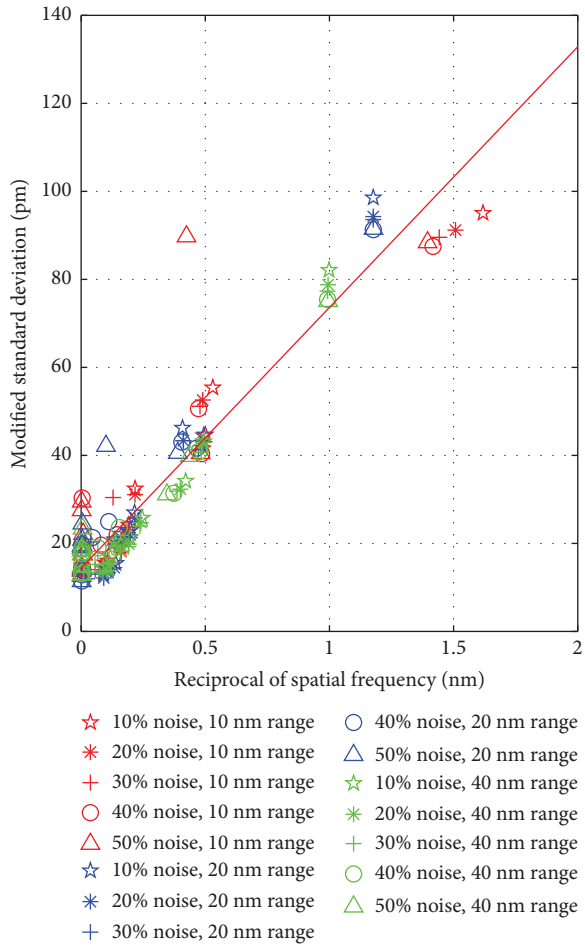

FIGURE 6: The relationship between the reciprocal of spatial frequency and the modified standard deviation of the cross-correlation method. The noise levels are 0%, 10%, 20%, 30%, 40%, and 50%. The spectral wavelength ranges are 10 nm, 20 nm, and 40 nm. The red line shows the linear fitting results [45].

$$D = \frac{1}{\sqrt{\mathrm{SNR}_L}}\left[59.2457\frac{W}{P} + 14.3808\right]. \tag{12}$$

Equation (12) may be used for fast evaluation of the influence of the noise level, from the spectral range for the detection, and the intended gauge lengths.

It has been shown that there is an approximately linear relationship between the spatial frequency and the gauge length. According to the definition of the spatial frequency in this paper, the mean spatial frequency of the cases shown in Figure 5 for the noise level of 0% is shown in Figure 7. The response of the spatial frequency to the gauge length is about 10 nm/cm. The red line shown in Figure 7 shows a linear function with a slope of 10 nm/cm and passing through the origin.

Then, with this approximated slope value, equation (12) can be adjusted as ($R^2 = 0.8602$):

$$D = \frac{1}{\sqrt{\mathrm{SNR}_L}}\left[\frac{5.9246}{L} + 14.3808\right], \tag{13}$$

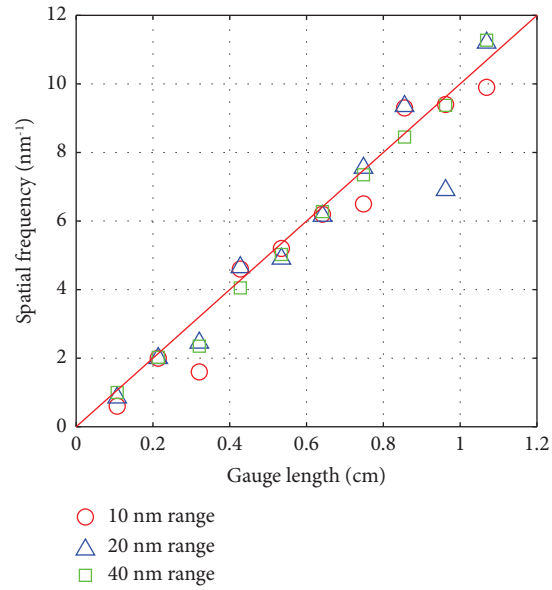

FIGURE 7: The relationship between the gauge length and the spatial frequency. The spectral wavelength ranges are 10 nm, 20 nm, and 40 nm. The red line shows the tendency [45].

where L is the gauge length in centimetres. It can be seen from, equation (13) that the standard deviation is proportional to the reciprocal of the square root of SNR. By increasing the SNR, the precision of strain detection will be improved.

If the sensitivity is defined as the value of the minimum input strain when the signal-to-noise ratio of strain (SNR_ε) equals 1, then a sensitivity (S) is equal to the deviation D in noise signals as follows:

$$S = \frac{1}{\sqrt{\mathrm{SNR}_L}}\frac{[5.9246/L + 14.3808]\,[\mu\varepsilon]}{1.24}, \tag{14}$$

when the responsivity is set at 1.24 pm/$\mu\varepsilon$. If the photon noise obeys a Poisson distribution and the light intensity is proportional to the gauge lengths, then the sensitivity formula can be expressed as

$$S = \frac{1}{\sqrt{\mathrm{SNR}_{L_0} \times L/L_0}}\frac{[5.9246/L + 14.3808]\,[\mu\varepsilon]}{1.24}, \tag{15}$$

where SNR_{L_0} is the signal-to-noise ratio of the spectra for the calibration gauge length of L_0.

4.2. Strain Measurement Application (An Aerospace Case). SHM integrates sensors within structures to record damage evolution and provides information for structural integrity analysis. The integrated sensor can perform real-time monitoring of structures, and that may reduce non-destructive evaluation frequency and thus decrease maintenance cost as well as increase structural life safety, which is vital in areas such as aerospace engineering [46]. Sensors can

be mounted on structures externally or embedded within structures [47]. Both internal and external sensors can be utilized for strain measurement.

Aluminium is a material widely used in aerospace engineering. FOS was integrated into an aluminium alloy part to analyse the influence of the position of the optical fibre sensor in a capillary [48]. The material of the aluminium alloy chosen was AlSi10Mg because AlSi10Mg has the advantage of good strength and low weight properties. It is often used for additive manufacturing in aircraft [49] and the specimen was manufactured with selective laser melting. The embedded optical fibre sensor was used to monitor the strain information to record damage evolution and to provide information for structural integrity analysis.

In order to make a comparison between the simulated results of the NP-doped optical fibre and commercial optical fibres, an experiment of an aerospace case was implemented to obtain real strain data. A set of experimental strain data was obtained from a commercial optical fibre sensor which was interrogated by the LUNA system (ODISI-B) at DASML of TU Delft.

Figure 8 shows a photo of the experimental setup used for monitoring the crack propagation with a four-point bending test. The aluminium alloy part was installed on a fatigue test machine (MTS servo-hydraulic test frame). The optical fibre sensor was embedded into the capillary of the aluminium alloy with injected adhesives. An initial notch was made at the middle of the bottom of the specimen. By loading of 8 kN employed on the specimen, the crack initiated and propagated. More detail of the structure of the specimen is shown in Figure 9.

Figure 9 shows the structure of the specimen on the four-point bending fatigue test machine. There is a cylindrical capillary with a 3 mm diameter (between the white dashed lines). The centre of the capillary is about 16 mm to the bottom of the specimen. Force was applied on the top of the specimen and two holders supported the specimen under loading. The initial notch position is shown in Figure 9.

Generally, when the crack is generated close to the optical fibre sensor, the local stress will cause a local strain change. By analysing the local strain distribution, the crack could be monitored. Figure 10 shows the experimental results of strain distributions in the optical sensing fibre for different crack lengths (crack lengths: 2 mm, 4 mm, 8 mm in blue, yellow, and green, respectively). The data were averaged from 100 testing results. The crack length was defined as the distance between the end of the crack to the bottom of the specimen. It can be seen that there is a peak in the middle of the sensing fibre and the peak increases when the crack propagates from 2 mm in length to 8 mm in length under load. When the crack length is small, for example, 2 mm, the shape change from the original uniformed strain is relatively small and it is comparable to the standard deviations (red bars). This makes it difficult to detect small cracks from the strain distribution pattern.

However, this drawback will be overcome when the backscattered light enhancement methods are used. The sensitivity of the strain sensing will increase when the

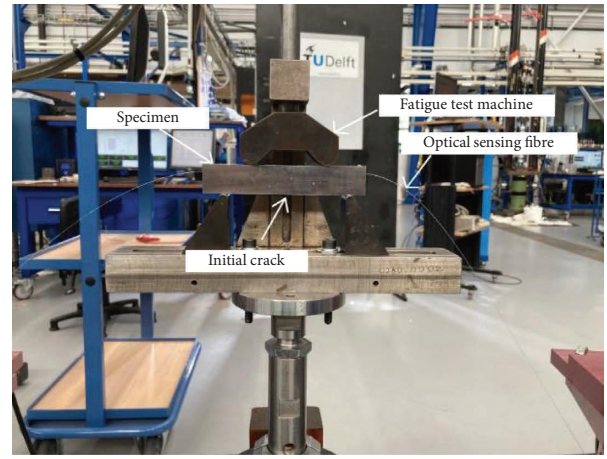

Figure 8: A photo of the experimental setup used for crack generation and detection. An optical fibre was embedded into the additive-manufactured aluminium alloy specimen to obtain strain data under loading tests. The optical fibre was connected to LUNA system.

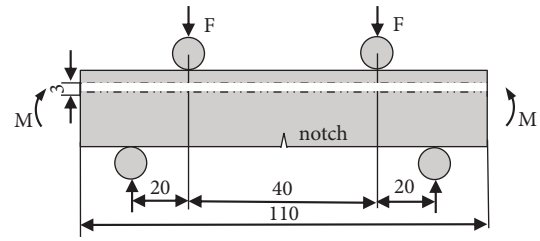

Figure 9: The structure of the specimen on the four-point bending fatigue test machine. The white dash hollow region is the capillary with 3 mm diameter. The optical fibre sensor was installed in the middle of the capillary but it is not shown in this figure.

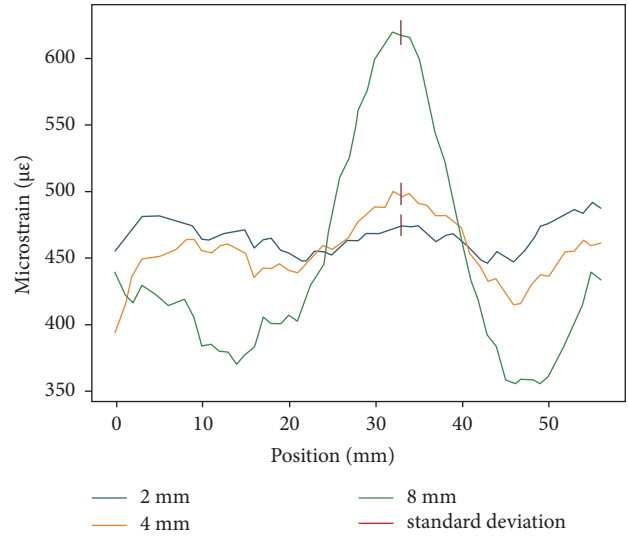

Figure 10: The experimental results of strain distributions in the optical sensing fibre for different crack lengths (2 mm, 4 mm, and 8 mm in blue, yellow, and green, respectively) from LUNA ODISI-B. The crack lengths are the distances between the end of the crack to the bottom of the specimen [45].

backscattered light increases. By ultraviolet (UV) light exposure, the backscattered light in single mode fibre −28 (SMF-28) will increase by 20 dB [24]. With nanoparticle doping, more than 40 dB backscattered light increase has been achieved [27, 29]. The obtained standard deviations of strain from the experiment are about 11 $\mu\epsilon$ from the commercial optical fibre. From equation (14), the strain standard deviations obtained from NP-doped optical fibres can be lower than that obtained from commercial single-mode optical fibres when the SNR_{L_0} is above 19 for a gauge length of 0.13 cm (L_0) and it will be easy to achieve a SNR_{L_0} of more than 19 with these backscattered light enhancement methods because of the dramatically increased backscattered light intensity.

Figure 11 shows a comparison between the simulated results and the experimental results from this work and the data from Loranger et al.'s paper [24]. The black star shown in Figure 11 is the experimental result from this work, which was obtained based on the experimental data for the standard deviation (11 $\mu\epsilon$) obtained from strain monitoring in Figure 10. The calibrated calculated sensitivity curve is shown in a blue line using this experimental data ($\mathrm{SNR}_{L_0} = 19$ for 0.13 cm gauge length (L_0)). The formula of the curve is $S = 0.3919/L^{3/2} + 0.9513/L^{1/2}$. The blue circles represent the sample points that were used as typical gauge lengths in previous sections which are 0.1069 cm, 0.2138 cm, 0.3207 cm, 0.4276 cm, 0.5345 cm, 0.6414 cm, 0.7483 cm, 0.8552 cm, 0.9621 cm, and 1.0690 cm, respectively.

The experimental data from Loranger et al.'s paper [24] are used for comparison. Loranger et al. obtained temperature measurements with the distributed fibre optic sensing for different gauge lengths which are 0.05 cm, 0.1 cm, 0.2 cm, 0.5 cm, 1.0 cm, 2.0 cm, and 10.0 cm, respectively. The calibration factor for strain and temperature used was 8.32 $\mu\epsilon/^{\circ}$C [24]. With this calibration factor, the sensitivities for strain measurement were obtained for these gauge lengths (shown in the red triangles). Compared with the experimental data, the sensitivity curve (in blue line) shows the same tendency and matches the experimental data from Loranger et al.'s paper [24].

4.3. Results of the New Proposed Method. The errors of the obtained spectral shifts are related to the spectral range as shown before (see Figure 5(a)) and the spatial frequency is proportional to the spectral range [34]. Therefore, increasing the spatial frequency from the original spectrum may increase the acquisition of the accuracy of the spectral shift and then increase the accuracy of the strain measurement. The new method was proposed based on these findings.

Figure 12 shows the results of the proposed method with the comparison from the cross-correlation method. The spectral range used was from 1540 nm to 1560 nm in Figure 12. The strain was set at 500 $\mu\epsilon$. The gauge lengths were set at 0.1069 cm, 0.2138 cm, 0.3207 cm, 0.4276 cm, 0.5345 cm, 0.6414 cm, 0.7483 cm, 0.8552 cm, 0.9621 cm, and 1.0690 cm.

In order to show the accuracy improvement with the proposed method compared with the traditional cross-correlation method, the error ratio was used in Figure 12, which is defined as the ratio of the relative error between the spectral shift calculated by the proposed method and the theoretical value to the relative error between the spectral shift calculated by the cross-correlation method and the theoretical value.

Figures 12(a) and 12(b) show the relative errors between the results calculated with the cross-correlation method and theoretical values in blue lines with circles and the relative errors between the results calculated with the proposed method and theoretical values in red lines with stars under noise levels of 0% and 10%, respectively. The errors decrease to half of their values for short gauge lengths when the proposed method is used. For longer gauge lengths, the improvement is not noticeable. Comparing Figures 12(a) and 12(b), it seems that the errors are reduced at some gauge lengths when there is noise. The reason is that the theoretical result was assumed as the true value for all wavelengths but it can only be used as the theoretical result at 1550 nm incident light wavelength, and the error defined is sensitive to the theoretical result that was chosen. The noise used in the simulation may shorten the mean values from the mean simulated result to the theoretical result.

To show the change of the spatial frequencies, the period ratio which was defined as the ratio of the spatial frequency with the proposed method to the original spatial frequency is used in the red lines in Figures 12(c) and 12(d) correspondingly. The blue lines in Figures 12(c) and 12(d) show the error ratios between the two methods. The tendency of the error ratio increases when the gauge length increases and the decreasing tendency of the period ratio confirm the idea of increasing the accuracy of the strain detection by increasing the spatial frequency with noise level 0. The period ratios are between 100% and 150%. The small increase of the spatial frequency indicates that the new characteristics of the spectra generated by the proposed method only increase the high spatial frequency components slightly and the increased high spatial frequency components have a difficulty to be distinguished from the noise if the noise level increases. As shown in Figure 12(d), the error ratios can be above 100% when there is 10% noise, which indicates that the proposed method is sensitive to noise but is beneficial to strain detection at short gauge lengths for low noise levels.

In summary, the characteristic spectral peaks within the measured spectral range are important for the spectral shift measurement under strain for NP-doped optical fibre sensing, especially for small gauge lengths because the backscattered light spectra show fewer characteristic spectral peaks for smaller gauge lengths compared with the cases for the larger gauge lengths as shown in Figure 7 (for the gauge length of about 0.1 cm gauge length cases, the spatial frequency is only about $1/\mathrm{nm}^{-1}$ which is 10 times lower than the cases for the gauge length of about 1 cm cases). With the newly proposed method, the accuracy of strain measurement will increase because of the increase in the characteristic spectral peaks. Therefore, the new method reduces the difficulty of tracking the spectral shift for the small gauge lengths. However, it needs to be noticed that the new spectra will be more sensitive to the noise because the signal decreases and it may not be obviously beneficial for cases for

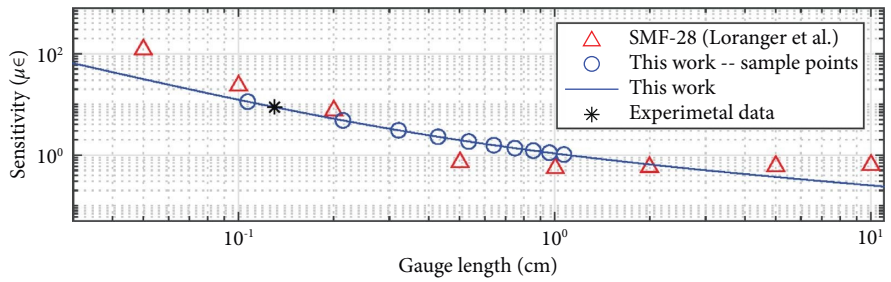

FIGURE 11: Comparison between simulated results and the experimental data. The results of single mode fibre −28 (SMF-28) [24] are in red triangles. The blue curve shows the calculated results with the sensitivity formula in this work and the blue dots show the gauge lengths used for simulations. The black star shows the experimental results from strain monitoring [45].

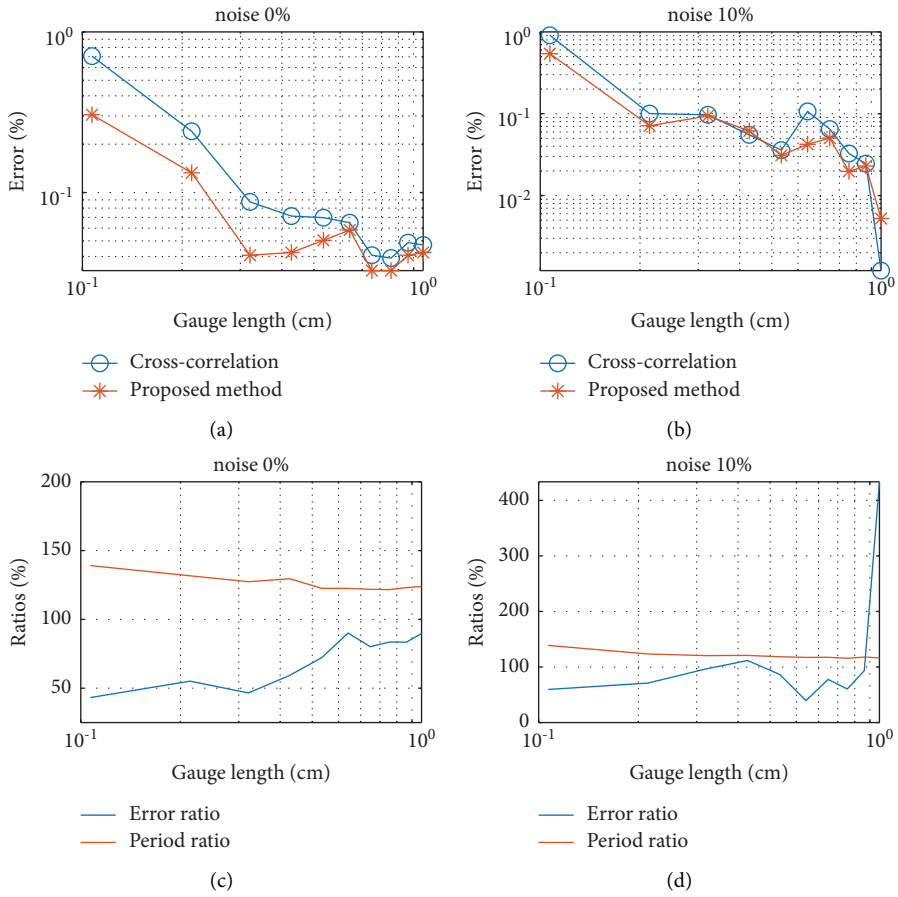

FIGURE 12: Comparisons between the proposed method and the traditional cross-correlation method at a strain value of 500 $\mu\epsilon$ and for a spectral range from 1540 nm to 1560 nm. The relative errors between mean values of the 100 cases and the true values with the improved cross-correlation method and traditional cross-correlation method under a noise level of (a) 0% and (b) 10%. The error ratios between the proposed method and traditional cross-correlation method and the corresponding spatial frequency ratios under a noise level of (c) 0% and (d) 10% [45].

the large gauge lengths which may have sufficient characteristic spectral peaks for the spectral tracking with the cross-correlation method.

5. Conclusions

A case study of the strain acquisition for the NP-doped optical fibre has been investigated with the traditional cross-correlation method. The expressions for the standard deviation of the acquired spectral shift and the sensitivity were obtained which can be used for fast calculating different sensors' gauge lengths and signal-to-noise ratios and spectral detection ranges. Compared with the traditional cross-correlation method, the proposed method is a simple further step which has the ability to reduce the errors by 50% to improve the accuracy of the spectral shift acquisition. The NP-doped optical fibre sensors provide highly backscattered light signals in the core of the optical fibre and the higher

sensitivity and accuracy strain detection may be used and be beneficial for strain monitoring for the critical positions for crack detection in aircraft structures.

Data Availability

The data used to support the findings of this study are available from the corresponding author upon reasonable request.

Conflicts of Interest

The authors declare that they have no conflicts of interest.

Authors' Contributions

X.W. and R.M.G. conceptualized the study. X.W. and R.M.G. proposed the methodology and provided software. X.W. contributed to validation, performed formal analysis, performed investigation, and wrote the original draft. (The aerospace case part was prepared with Y.X. based on Y.X. and C.R.'s project). X.W., Y.X., C.R., R.B., and R.M.G. reviewed and edited the article X.W. and Y.X. contributed to visualization. R.M.G., C.R., and R.B. performed supervision. R.M.G. provided project administration. All authors reviewed the manuscript.

Acknowledgments

X.W. gratefully acknowledges financial support from the China Scholarship Council (No. 201806020197) and Y.X. gratefully acknowledges financial support from the China Scholarship Council (No. 201706020152).

References

[1] A. Bassil, X. Chapeleau, D. Leduc, and O. Abraham, "Concrete crack monitoring using a novel strain transfer model for distributed fiber optics sensors," *Sensors*, vol. 20, no. 8, p. 2220, 2020.

[2] A. Kesavan, S. John, and I. Herszberg, "Strain-based structural health monitoring of complex composite structures," *Structural Health Monitoring*, vol. 7, no. 3, pp. 203–213, 2008.

[3] R. Di Sante, "Fibre optic sensors for structural health monitoring of aircraft composite structures: recent advances and applications," *Sensors*, vol. 15, no. 8, pp. 18666–18713, 2015.

[4] M. Ramakrishnan, G. Rajan, Y. Semenova, and G. Farrell, "Overview of fiber optic sensor technologies for strain/temperature sensing applications in composite materials," *Sensors*, vol. 16, no. 1, p. 99, 2016.

[5] A. Boersma, R. Cremers, and R. Jansen, "Fiber Bragg grating distributed chemical sensors," *Procedia Engineering*, vol. 168, pp. 1245–1248, 2016.

[6] M. R. Samsudin, Y. G. Shee, F. R. Mahamd Adikan, B. B. Abdul Razak, and M. Dahari, "Fiber Bragg gratings hydrogen sensor for monitoring the degradation of transformer oil," *IEEE Sensors Journal*, vol. 16, no. 9, pp. 2993–2999, 2016.

[7] X. Liu, B. Jin, Q. Bai, Y. Wang, D. Wang, and Y. Wang, "Distributed fiber-optic sensors for vibration detection," *Sensors*, vol. 16, no. 8, p. 1164, 2016.

[8] S. C. M. Ho, W. Li, B. Wang, and G. Song, "A load measuring anchor plate for rock bolt using fiber optic sensor," *Smart Materials and Structures*, vol. 26, no. 5, Article ID 057003, 2017.

[9] F. G. Yuan, *Structural Health Monitoring (SHM) in Aerospace Structures*, Woodhead Publishing, Delhi, India, 2016.

[10] S. Goossens, B. De Pauw, T. Geernaert et al., "Aerospace-grade surface mounted optical fibre strain sensor for structural health monitoring on composite structures evaluated against in-flight conditions," *Smart Materials and Structures*, vol. 28, no. 6, Article ID 065008, 2019.

[11] Y. W. Sasy Chan, H. P. Wang, and P. Xiang, "Optical fiber sensors for monitoring railway infrastructures: a review towards smart concept," *Symmetry*, vol. 13, no. 12, p. 2251, 2021.

[12] H. P. Wang, P. Xiang, and L. Z. Jiang, "Optical fiber sensing technology for full-scale condition monitoring of pavement layers," *Road Materials and Pavement Design*, vol. 21, no. 5, pp. 1258–1273, 2018.

[13] M. Froggatt and J. Moore, "High-spatial-resolution distributed strain measurement in optical fiber with Rayleigh scatter," *Applied Optics*, vol. 37, no. 10, pp. 1735–1740, 1998.

[14] L. Fazzi, N. Dias, M. Holynska, A. Tighe, R. Rampini, and R. M. Groves, "Monitoring of silicone adhesive in space solar cells with an embedded multi-parameter TFBG sensor in a simulated space environment," *Measurement Science and Technology*, vol. 33, no. 8, Article ID 085108, 2022.

[15] L. Fazzi, G. Struzziero, C. Dransfeld, and R. M. Groves, "A single three-parameter tilted fibre Bragg grating sensor to monitor the thermosetting composite curing process," *Advanced Manufacturing: Polymer and Composites Science*, vol. 8, no. 1, pp. 33–41, 2022.

[16] W. Eickhoff and R. Ulrich, "Optical frequency domain reflectometry in single-mode fiber," *Applied Physics Letters*, vol. 39, no. 9, pp. 693–695, 1981.

[17] Z. Ding, C. Wang, K. Liu et al., "Distributed optical fiber sensors based on optical frequency domain reflectometry: a review," *Sensors*, vol. 18, no. 4, p. 1072, 2018.

[18] J. Song, W. Li, P. Lu, Y. Xu, L. Chen, and X. Bao, "Long-range high spatial resolution distributed temperature and strain sensing based on optical frequency-domain reflectometry," *IEEE Photonics Journal*, vol. 6, no. 3, pp. 1–8, 2014.

[19] S. T. Kreger, I. I. I. O. J. Ohanian, N. Garg et al., "Optical frequency domain reflectometry for aerospace applications," in *Fiber Optic Sensors and Applications XIV*Vol. 10208, International Society for Optics and Photonics, Bellingham, DC, USA, 2017.

[20] Y. Shan, H. Xu, Z. Zhou, Z. Yuan, X. Xu, and Z. Wu, "State sensing of composite structures with complex curved surface based on distributed optical fiber sensor," *Journal of Intelligent Material Systems and Structures*, vol. 30, no. 13, pp. 1951–1968, 2019.

[21] H. Murayama, D. Wada, and H. Igawa, "Structural health monitoring by using fiber-optic distributed strain sensors with high spatial resolution," *Photonic Sensors*, vol. 3, no. 4, pp. 355–376, 2013.

[22] H. Wang, L. Jiang, and P. Xiang, "Improving the durability of the optical fiber sensor based on strain transfer analysis," *Optical Fiber Technology*, vol. 42, pp. 97–104, 2018.

[23] H. Wang, P. Xiang, and L. Jiang, "Strain transfer theory of industrialized optical fiber-based sensors in civil engineering: a review on measurement accuracy, design and calibration," *Sensors and Actuators A: Physical*, vol. 285, pp. 414–426, 2019.

[24] S. Loranger, M. Gagné, V. Lambin-Iezzi, and R. Kashyap, "Rayleigh scatter based order of magnitude increase in

distributed temperature and strain sensing by simple UV exposure of optical fibre," *Scientific Reports*, vol. 5, no. 1, pp. 11177–7, 2015.

[25] P. Lu, S. J. Mihailov, D. Coulas, H. Ding, and X. Bao, "Low-loss random fiber gratings made with an fs-IR laser for distributed fiber sensing," *Journal of Lightwave Technology*, vol. 37, no. 18, pp. 4697–4702, 2019.

[26] F. Parent, S. Loranger, K. K. Mandal et al., "Enhancement of accuracy in shape sensing of surgical needles using optical frequency domain reflectometry in optical fibers," *Biomedical Optics Express*, vol. 8, no. 4, pp. 2210–2221, 2017.

[27] D. Tosi, C. Molardi, and W. Blanc, "Rayleigh scattering characterization of a low-loss MgO-based nanoparticle-doped optical fiber for distributed sensing," *Optics and Laser Technology*, vol. 133, Article ID 106523, 2021.

[28] V. Fuertes, N. Grégoire, P. Labranche et al., "Engineering nanoparticle features to tune Rayleigh scattering in nanoparticles-doped optical fibers," *Scientific Reports*, vol. 11, no. 1, pp. 9116–9212, 2021.

[29] V. Fuertes, N. Grégoire, S. Morency et al., "Tunable distributed sensing performance in Ca-based nanoparticle-doped optical fibers," *Optical Materials Express*, vol. 12, no. 4, pp. 1323–1336, 2022.

[30] X. Wang, R. Benedictus, and R. M. Groves, "Optimization of light scattering enhancement by gold nanoparticles in fused silica optical fiber," *Optics Express*, vol. 29, no. 13, pp. 19450–19464, 2021.

[31] V. Ewald, R. M. Groves, and R. Benedictus, "Transducer placement option of Lamb wave SHM system for hotspot damage monitoring," *Aerospace*, vol. 5, no. 2, p. 39, 2018.

[32] X. Wang, R. Benedictus, and R. M. Groves, "Modelling of light scattering by gold nanoparticles at optical fibre interfaces," *Journal of Optics*, vol. 23, no. 3, Article ID 035602, 2021.

[33] X. Wang, R. Benedictus, and R. M. Groves, "Plasmon resonance based gold nanoparticle doped optical fibre strain sensing," *Optics and Laser Technology*, vol. 153, Article ID 108272, 2022.

[34] X. Wang, R. Benedictus, and R. M. Groves, "Spectral characteristics of gold nanoparticle doped optical fibre under axial strain," *Scientific Reports*, vol. 12, no. 1, Article ID 16593, 2022.

[35] A. Yan, S. Huang, S. Li et al., "Distributed optical fiber sensors with ultrafast laser enhanced Rayleigh backscattering profiles for real-time monitoring of solid oxide fuel cell operations," *Scientific Reports*, vol. 7, no. 1, p. 9360, 2017.

[36] C. Molardi, S. Korganbayev, W. Blanc, and D. Tosi, "Characterization of a nanoparticles-doped optical fiber by the use of optical backscatter reflectometry," in *Advanced Sensor Systems and Applications VIII. 10821*, International Society for Optics and Photonics, Bellingham, DC, USA, 2018.

[37] Luna User's Guide, "LUNA user's guide— ODiSI-B version 5.2.1," https://lunainc.com/sites/default/files/assets/files/resource-library/ODiSI-B-Users-Guide.pdf.

[38] H. Murayama, K. Ohara, N. Kanata, K. Kageyama, and H. Igawa, "Strain monitoring and defect detection in welded joints by using fiber-optic distributed sensors with high spatial resolution," *E-Journal of Advanced Maintenance*, vol. 2, no. 3, pp. 191–199, 2011.

[39] M. Zhu and H. Murayama, "Fast demodulation of OFDR based long length FBG sensing system for noisy signals," *Optics Express*, vol. 26, no. 16, pp. 19804–19814, 2018.

[40] S. T. Kreger, A. K. Sang, D. K. Gifford, and M. E. Froggatt, "Distributed strain and temperature sensing in plastic optical fiber using Rayleigh scatter," in *Fiber Optic Sensors and Applications VI*,vol. 7316, p. 73160A, International Society for Optics and Photonics, Bellingham, DC, USA, 2009.

[41] Z. Guo, J. Yan, G. Han, D. Greenwood, J. Marco, and Y. Yu, "High sensing accuracy realisation with millimetre/sub-millimetre resolution in optical frequency domain reflectometer," *Journal of Lightwave Technology*, vol. 40, no. 12, pp. 4050–4056, 2022.

[42] Z. Zhou, C. Chen, P. Lu, S. Mihailov, L. Chen, and X. Bao, "Random fiber grating characterization based on OFDR and transfer matrix method," *Sensors*, vol. 20, no. 21, p. 6071, 2020.

[43] E. Li, "Rayleigh scattering based distributed optical fiber sensing," in *AOPC 2017 Fiber Optic Sensing and Optical Communications*,vol. 10464, p. 104641K, International Society for Optics and Photonics, Bellingham, DC, USA, 2017.

[44] P. Vlugter and Y. Bellouard, "Elastic properties of self-organized nanogratings produced by femtosecond laser exposure of fused silica," *Physical Review Materials*, vol. 4, no. 2, Article ID 023607, 2020.

[45] X. Wang, *Development of highly scattering distributed fibre optic sensing for structural health monitoring*, PhD thesis, Delft University of Technology, Delft, Netherlands, 2023.

[46] D. Inaudi and B. Glisic, *Fibre Optic Methods for Structural Health Monitoring*, John Wiley & Sons, Hoboken, NJ, USA, 2008.

[47] F. K. Chang, J. F. C. Markmiller, J. Yang, and Y. Kim, *Structural Health Monitoring*, John Wiley & Sons, Hoboken, NJ, USA, 2011.

[48] Y. Xiao, C. Rans, D. Zarouchas, and R. Benedictus, "Measurement accuracy of distributed sensing fibers embedded within capillaries of solid structures," in *Proceedings of the 12th International Workshop on Structural Health Monitoring: Enabling Intelligent Life-Cycle Health Management for Industry Internet of Things (IIOT)*, vol. 32290, pp. 1645–1652, IWSHM, Stanford University, CA, USA, November 2019.

[49] K. Kempen, L. Thijs, J. Van Humbeeck, and J. P. Kruth, "Mechanical properties of AlSi10Mg produced by selective laser melting," *Physics Procedia*, vol. 39, pp. 439–446, 2012.